SEMARAK ILMU PUBLISHING

Journal of Advanced Research in Applied Sciences and Engineering Technology

Journal homepage:
https://semarakilmu.com.my/journals/index.php/applied_sciences_eng_tech/index
ISSN: 2462-1943

Optimization and Modelling to Enhance Hydroturbine Performance

Daniyar Bossinov[1,*], Gaukhar Ramazanova[1], Dinara Turalina[2]

[1] Satbayev University, Almaty, Kazakhstan
[2] Al-Farabi Kazakh National University, Almaty, Kazakhstan

ARTICLE INFO

Article history:
Received 2 October 2023
Received in revised form 4 March 2024
Accepted 6 May 2024
Available online 20 June 2024

Keywords:

Sustainable energy; Hydroturbine; Blade design; Power; Efficiency

ABSTRACT

In this study, a new design of a hydroturbine was developed, modelled, and constructed. The unique features of this turbine design required a thorough investigation and optimization process to enhance hydroturbine performance. The paper discusses numerical and experimental results obtained on the hydroturbine. The optimal angle of attack for the inlet flow direction has been computed from numerical modelling. Consequently, data on velocity, pressure, lift, and drag forces along the blade have been obtained. The study also takes into account the operation of the hydroturbine under non-rotating and rotating rotor modes. Performance metrics such as head, torque, hydraulic power, hydroturbine power, and efficiency were then calculated based on water discharge. These performance calculations were conducted using COMSOL Multiphysics, employing Direct Numerical Simulation and k-epsilon methods. Numerical calculations offer a cost-effective approach to reducing the financial burden associated with material costs for manufacturing hydroturbine prototypes.

1. Introduction

The significance of this scientific research is closely tied to the advancement of renewable energy sources, particularly within the domain of hydroturbines, which play a crucial role in the realm of renewable energy.

This hydroturbine distinguishes itself from existing designs due to its unique features, necessitating an investigation and optimization process to improve its performance. The distinctiveness of the hydroturbine design makes it challenging to directly compare the obtained numerical and experimental results with those of other authors' works. Therefore, the results derived from this study are specific and exclusive to this particular hydroturbine design. The goal of numerical modelling and experimental testing on the hydroturbine is to improve its performance.

* *Corresponding author.*
E-mail address: dansho.91@mail.ru

https://doi.org/10.37934/araset.47.1.8193

1.1 Literature Review

Hydropower, both large and small, remains the primary global renewable energy source for electricity. According to Dametew [1], small hydroelectric power plants, often known as "run-of-the-river" installations without dams, prove to be both cost-effective and environmentally friendly. They are particularly effective for rural electrification in developing countries and are also viable options for expanding hydropower projects in developed nations. Onyemaechi *et al.,* [2] highlighted that small hydro technology exhibits remarkable resilience and is recognized as one of the most environmentally friendly energy technologies currently available. Igbinovia *et al.,* [3] noted that during the 20th century, the expansion of hydropower was linked to the building of large dams. While these dams offered substantial benefits such as electricity supply, irrigation, and flood control, they also led to the submersion of fertile land and the displacement of local populations. In many instances, dams quickly accumulate silt, diminishing their effectiveness and lifespan while also causing environmental issues due to substantial disruption of river flows. Small hydraulic systems, typically "run-of-river" setups, consist of small dams or dams with limited or no water storage, as depicted in the research by Musa *et al.,* [4].

2. Methodology

2.1 Hydroturbine Overview

The hydroturbine operates in the following manner: the water enters from the inlet and passes through the swirler, which rotates the water direction to the blades. The water flows then act on the blades and create lift and drag forces, which rotate the rotor along the z-axis, after which the water exits through the outlet (Figure 1(a) and 1(b)). Due to the rotation of the magnets, which are located in the rotor, the hydroturbine produces electricity in its magnet wire.

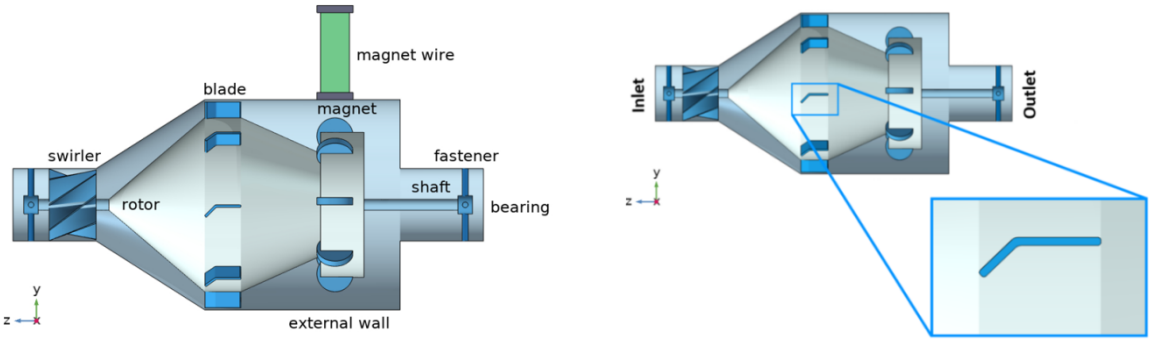

(a) (b)

Fig. 1. (a) Transparent view (b) Selected domain

2.2 Modelling of a Two-Dimensional Domain

The Navier-Stokes equations presented in the following works [5-10] are used to solve a two-dimensional domain under the laminar flow mode:

Conservation of mass equation:

$$\nabla \cdot u = 0 \tag{1}$$

Momentum equation:

$$\rho\left(\frac{\partial u}{\partial t}+u\cdot\nabla u\right)=-\nabla p\cdot+\nabla\cdot(\mu(\nabla u+(\nabla u)^{T})] \tag{2}$$

here u denotes the velocity, ρ is the density, μ is the dynamic viscosity, and p is the pressure.

The direct numerical simulation method is employed for a two-dimensional domain, offering enhanced accuracy in comparison to alternative approaches.

When solving a task, the part of the rotor where the blade is located was chosen for two-dimensional calculations (Figure 1(b)).

Figures 2(a) and 2(b) show the boundary conditions and mesh distribution of the two-dimensional domain, respectively.

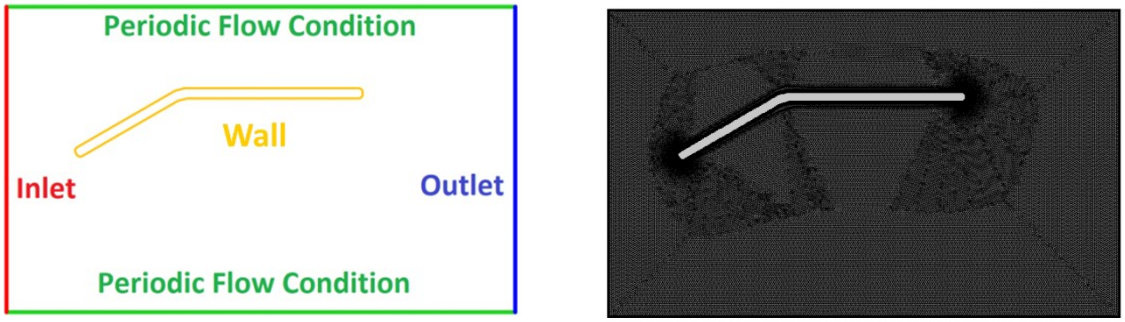

(a) (b)

Fig. 2. (a) Boundary conditions (b) Mesh distribution

Two methods exist for altering the angle of attack of the swirler. One method entails rotating the blade itself, whereas the alternative method involves maintaining the blade in a fixed position but adjusting the flow direction at the inlet, as demonstrated in the paper [11]. In the numerical computation provided, the latter method is employed. Modifying the velocity direction at the inlet is much simpler in this scenario, as there is no requirement to remesh the task for each angle of attack. As depicted in Figure 3(a), the blade remains fixed while the arrows illustrate the flow at an angle of attack of 45^0 due to the altered inlet velocity direction.

The rectangular domain measures 50 mm in length and 30 mm in height. As for the blade, its length is 28.25 mm, and its height is 2 mm. The velocity field at the inlet is specified in the x and y directions as $U\cdot\cos(\alpha\cdot\pi/180)$ and $U\cdot\sin(\alpha\cdot\pi/180)$, correspondingly. The magnitude of U is 1 m/s and the values of α consist of 0^0, 15^0, 30^0, 45^0, 60^0, 75^0, and 90^0. The "Periodic flow conditions" are applied to the lower and upper boundaries of the domain due to the influence of water velocity variations on both the lower and upper blades of the selected blade. The no-slip boundary condition is chosen for the blade wall. The outlet is specified with a pressure condition. The dynamic viscosity value is 0.001 $(Pa\cdot s)$ and the density value is 999.62 (kg/m^3).

The two-dimensional model is considered as non-stationary. The calculation continued until repeatable results were obtained, which required 10 seconds. The calculation results were recorded every 0.1 seconds.

Figure 3(a) displays the water flow passing the blade at a 45^0 angle of attack. The surface plot shows the magnitude of velocity, represented by arrows. The deep blue water colour indicates the presence of vortex and cavitation, whereas the deep red water colour indicates a significant increase in velocity. Figure 3(b) depicts the distribution of pressure, with a change in water color from deep blue to deep red signifying a noticeable pressure increase.

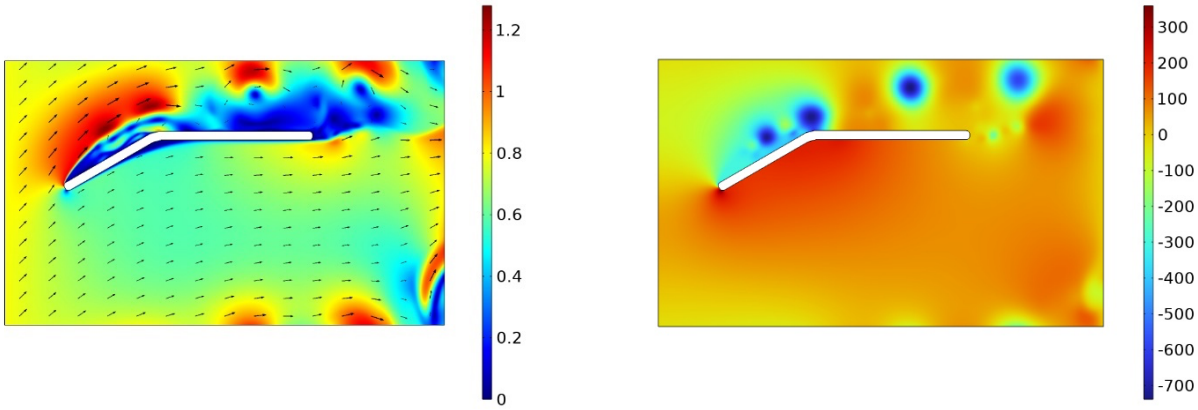

(a) (b)

Fig. 3. (a) Velocity value (m/s) (b) Pressure distribution (Pa)

2.2.1 Computing lift force and drag force

When a fluid flows around an object, it applies a force to the surface. Illustrated in the figures below, the force component perpendicular to the flow direction is termed as lift force, while the force component parallel to the flow direction is referred to as drag force. Figures 4(a) and 4(b) provide schematic representations of lift force and drag force, respectively.

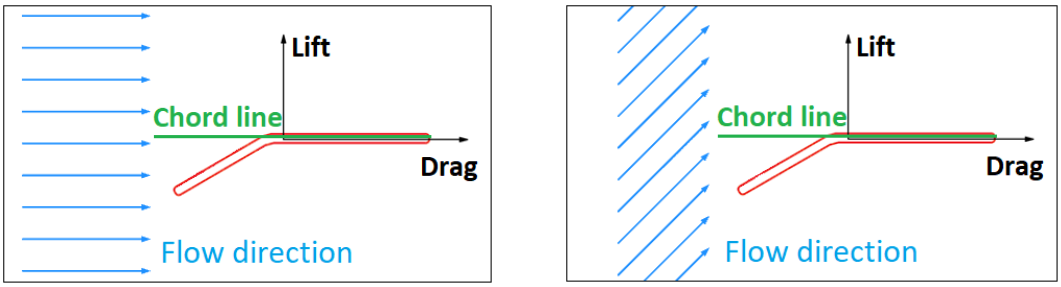

(a) (b)

Fig. 4. (a) Fluid flow at 0^0 angle of attack (b) Fluid flow at 45^0 angle of attack

In many cases, the geometry may not align perfectly with the flow direction. The angle formed between the centre reference line of the geometry and the incoming flow is known as the angle of attack. In aerospace engineering, the angle of attack is commonly utilized, as it represents the angle between the chord line of the air foil and the free-stream direction.

Lift and drag forces have two primary components — pressure and viscous forces. The pressure force, also known as the pressure-gradient force, arises from the pressure difference across the surface. On the other hand, the viscous force results from friction and opposes the flow direction. In 2D fluid flow, lift force and drag force expressions discussed in the references [6,7,11] are represented by Eq. (3) and Eq. (4), respectively:

$$F_L = \int_S (\rho\mu \frac{\partial u}{\partial n} n_x + p n_y) dS \tag{3}$$

$$F_D = \int_S (\rho\mu \frac{\partial u}{\partial n} n_y - p n_x) dS \quad (4)$$

Where n_x is the unit normal vector in the x direction, n_y is the unit normal vector in the y direction, and S is the boundary of the blade.

Figures 5(a) and 5(b) depict graphs showing variations in lift force and drag force over a 10-second timeframe resulting from alterations in water direction. The oscillations' frequency and amplitude in the figures below are attributed to flow perturbations induced by the vortices.

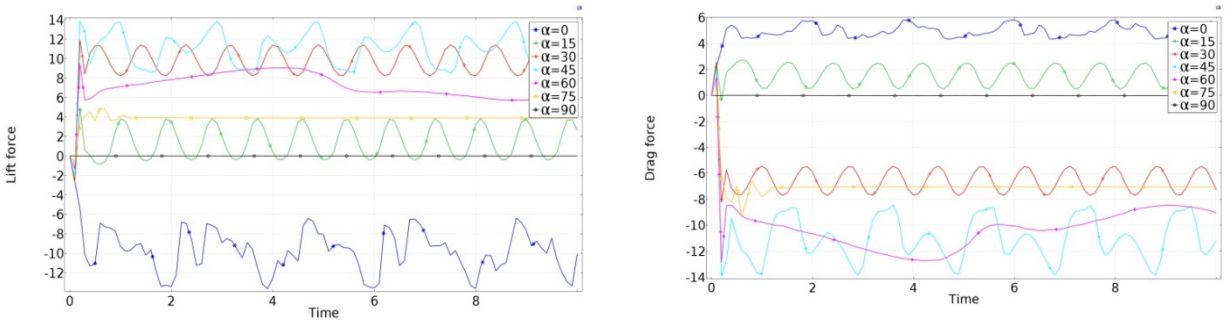

(a) (b)

Fig. 5. (a) Lift forces at different angles (b) Drag forces at different angles

In the calculations, the maximum lift force value was observed when the water flow direction was at 45^0. At angles of attack of 0^0 and 90^0, no lift force is present because water does not impact the lower surface of the blade. Between 75^0 and 90^0, a stall occurs due to a decrease in the lift force generated by the blade as the angle of attack increases. This phenomenon occurs when the blade's critical angle of attack is surpassed. Figure 5(b) shows that the maximum drag force is reached at a 0^0 angle of attack. Likewise, as seen in Figure 5(a), the drag force value at a 90^0 angle of attack is also zero. This occurs because there is no flow velocity present in the domain.

The definitions of lift and drag coefficients, as well as the results of these coefficients, are thoroughly explained in the previous study [12].

2.3 Modelling of Hydroturbine Performance

By conducting numerical computations on the 3D model of the operation of the hydroturbine, it becomes possible to observe the influence of water flow on the blades and the rotation of the rotor. The use of the 3D model for the hydroturbine renders the processes more realistic and achievable compared to the 2D model.

At a water flow direction of 45^0, the lift and drag forces reach their maximum and minimum values, respectively, as depicted in Figures 5(a) and 5(b). In this context, the swirler directions are set at 45^0, aligning with the angle of attack of the flow directed towards the blades at the same degree value.

To decrease the computation time, the following simplifications were implemented: the bearing, shaft, and fasteners were not taken into consideration for the task.

The inlet and outlet diameters of the hydroturbine are 0.1 m. The maximum diameter and length of the hydroturbine are 0.29 m and 0.65 m, respectively.

The fluid properties are identical in both the 2D and 3D models.

In the 3D model, the k-epsilon turbulence model was applied to solve the rotating and non-rotating modes of the hydroturbine rotor. The k-epsilon model stands out as one of the widely

adopted turbulence models in industrial contexts. This model includes the standard k-epsilon model, which is detailed in the works [8-10,13] and introduces two additional transport equations that operate with two dependent variables: the turbulent kinetic energy, denoted as k, and the turbulent dissipation rate, denoted as ε.

The transport equation is as follows:

$$\rho\frac{\partial k}{\partial t}+\rho u\cdot\nabla k=\nabla\cdot\left(\left(\mu+\frac{\partial\mu_T}{\sigma_k}\right)\nabla k\right)+P_k-\rho\varepsilon \tag{5}$$

Here the production term, P_k, is modelled as:

$$P_k=\mu_T\left(\nabla u:(\nabla u+(\nabla u)^T)-\frac{2}{3}(\nabla\cdot u)^2\right)-\frac{2}{3}\rho k\nabla\cdot u \tag{6}$$

The turbulent viscosity, μ_T, is described as:

$$\mu_T=\rho C_\mu\frac{k^2}{\varepsilon} \tag{7}$$

The transport equation, ε, is written in the following form:

$$\rho\frac{\partial\varepsilon}{\partial t}+\rho u\cdot\nabla\varepsilon=\nabla\cdot\left(\left(\mu+\frac{\mu_T}{\sigma_\varepsilon}\right)\nabla\varepsilon\right)+C_{\varepsilon1}\frac{\varepsilon}{k}P_k-C_{\varepsilon2}\rho\frac{\varepsilon^2}{k} \tag{8}$$

The constants of the k-epsilon model in Eq. (5), Eq. (7) and Eq. (8) are defined based on the experimental data, and their values are provided in Table 1.

Table 1
The values of constants

σ_k	σ_ε	C_μ	$C_{\varepsilon1}$	$C_{\varepsilon2}$
1.0	1.3	0.09	1.44	1.92

2.3.1 Modelling of the non-rotating rotor mode

The Reynolds number is calculated based on the inlet velocity and diameter, which in this instance are 0.79067 m/s (the eighth experiment in Table 3) and 0.1 m, respectively.

$$\mathrm{Re}=\frac{\rho\cdot U_i\cdot D_i}{\mu}=\frac{999.62\cdot0.79067\cdot0.1}{0.001}=79037 \tag{9}$$

Where U_i is the inlet velocity, D_i is the inlet diameter.

The high Reynolds number is a clear indicator of turbulent flow, necessitating the application of a turbulence model for accurate representation.

With the exception of the inlet and outlet boundaries, all other boundaries of the hydroturbine are walls. The walls have a no-slip boundary condition.

Figures 6(a) and 6(b) show the velocity streamlines and pressure distribution when the rotor is not rotating. The ribbon type was chosen to display the streamlines. The streamlines are color-coded based on the velocity magnitude, and their thickness is proportional to the turbulent viscosity, as shown in Figure 6(a) and 8(a). The broad lines suggest a high level of mixing. Mixing appears relatively weak at the front of the hydroturbine, but the plot indicates that it increases noticeably towards the rear of the hydroturbine. In addition, the velocity flow streamlines show that the swirler changes the direction of water flow. Initially, the direction of water flow velocity is perpendicular to the inlet boundary, after passing the swirler it changes its direction and swirls.

Bernoulli's principle states that an increase in fluid velocity leads to a decrease in pressure, and conversely, a decrease in velocity results in an increase in pressure. The solution clearly demonstrates that the observed pressure distribution aligns with this principle, as shown in Figures 6(b) and 8(b).

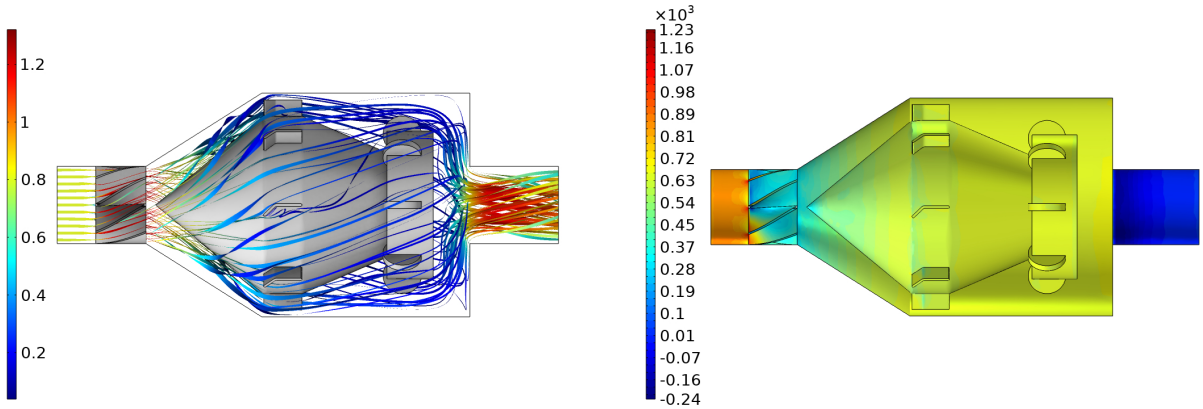

(a) (b)

Fig. 6. (a) Velocity streamlines (m/s) (b) Pressure distribution (Pa)

2.3.2 Modelling of the rotating rotor mode

The frozen rotor approach was used to solve the rotating mode. The frozen rotor method is a cost-effective and time-efficient steady-state approximation in which distinct zones are assigned different rotational speeds. The moving reference frame equations are employed to solve the flow within each of these zones. Essentially, this approach involves fixing the motion of the moving part in a specific position and then examining the resulting flow field with the rotor held in that fixed position.

The Navier-Stokes equations in the frozen rotor approach, which are detailed in the COMSOL Multiphysics User's Guide [10], will be in the following form:

Continuity equation:

$$\nabla \cdot (\rho v) = 0 \tag{10}$$

Momentum equation:

$$\rho(v \cdot \nabla) v + 2\rho\Omega \times v = \nabla \cdot [-p\mathrm{I} + \tau] + F - \rho\Omega \times (\Omega \times r) \tag{11}$$

Here ν denotes the velocity vector, Ω the angular velocity vector, I the identity matrix, τ the viscous stress tensor, F the volume force, and r the position vector.

All eight experiments listed in Table 3 were computed in the rotating mode. The calculations were performed for the head, torque, power, and efficiency of the hydroturbine (Table 2).

For a Newtonian fluid, the impeller Reynolds number defined by Paul *et al.,* [14] is as follows:

$$\mathrm{Re}_N = \frac{\rho \cdot N \cdot D_r^2}{\mu} \tag{12}$$

Where N is the rotations per second, D_r is the impeller diameter.

The head, which represents the difference in pressure head and velocity head between the inlet and outlet of the hydroturbine as water flows through it, as defined in the review papers by the authors [15,16], is given by the following expression:

$$H = \frac{\Delta p_{tot}}{\rho \cdot g} = \frac{\left(\left(p_i + \frac{\rho \cdot U_i^2}{2}\right) - \left(p_o + \frac{\rho \cdot U_o^2}{2}\right)\right)}{\rho \cdot g} = \frac{p_i - p_o}{\rho \cdot g} + \frac{U_i^2 - U_o^2}{2g} \tag{13}$$

Where Δp_{tot} denotes the total pressure difference between inlet and outlet boundaries, g the gravitational constant, p_i the inlet static pressure, p_o the outlet static pressure, U_i the inlet velocity, and U_o represents the outlet velocity.

The efficiency formula for the hydroturbine, as defined in the following works [17-19], is as follows:

$$\eta = \frac{P_t}{P_w} \cdot 100\% \tag{14}$$

Here P_t denotes the hydroturbine power, P_w is the hydraulic power input.

The hydroturbine power is defined by

$$P_t = \omega \cdot M \tag{15}$$

Where ω represents the angular velocity vector, M the torque.

The angular velocity is defined by

$$\omega = 2 \cdot \pi \cdot N \tag{16}$$

The torque is determined by

$$M = \left| \hat{z} \cdot \int_A r \times T dA \right| \tag{17}$$

Where A is the surface area of the rotor, T is the total stress, r is the point {x, y, z}, $\hat{z}$ is the direction of the rotation axis.

The hydraulic power input is determined by

$$P_w = Q \cdot H \cdot \rho \cdot g \tag{18}$$

Where Q is the water flow rate.

Figure 7(a) displays the head of the hydroturbine. Two plots are used to monitor the mass flow, one at the inlet and the other at the outlet. Figure 7(b) illustrates that the mass flow rates at the inlet and outlet are equal, indicating successful mass conservation. The dots represent the velocity values at the inlet.

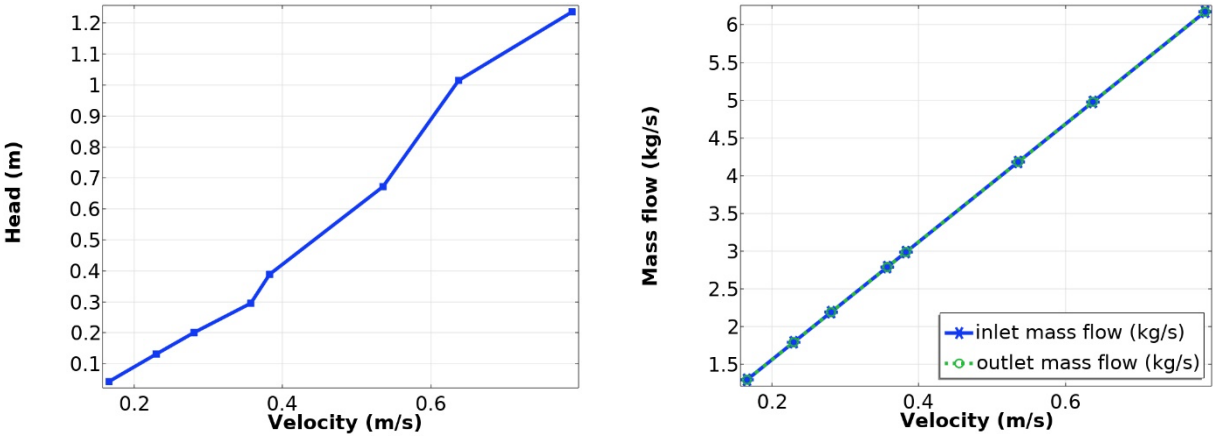

(a) (b)

Fig. 7. (a) Head (m) (b) Mass flow (kg/s)

Table 2 shows the computed results of the Reynolds number, impeller Reynolds number, head, torque, hydraulic power, hydroturbine power and efficiency.

Table 2
The calculated values of hydroturbine performance

No.	Inlet Velocity	Reynolds Number	Impeller Reynolds Number	Head m	Torque $N \cdot m$	Hydraulic Power W	Hydroturbine power W	Efficiency
1	0.16579	16573	8692	0.042545	0.041041	0.53995	0.12034	22.287
2	0.22955	22946	17073	0.13114	0.12950	2.3045	0.74588	32.367
3	0.28056	28045	21109	0.20069	0.19437	4.3103	1.3841	32.112
4	0.35708	35694	24834	0.29521	0.27574	8.0695	2.3101	28.627
5	0.38258	38243	29490	0.38889	0.36833	11.389	3.6643	32.173
6	0.53562	53541	37250	0.67207	0.61057	27.556	7.6726	27.843
7	0.63764	63739	46563	1.0151	0.91938	49.551	14.442	29.145
8	0.79067	79036	48115	1.2364	1.0867	74.834	17.639	23.571

To visualize the rotating mode of the hydroturbine rotor, the eighth experiment from Table 3 was selected, in which the velocity at the inlet is 0.79067 m/s and the rotor rotates at 155 revolutions per minute at the z-axis. Figure 8(a) illustrates the flow direction using the streamlines. As the streamlines traverse the rotor, they experience alterations due to circulation, which intensifies towards the rotor's end, eventually forming vortices. These vortices, in turn, trigger the cavitation process, leading to damage across the entire surface of the hydroturbine. In the rotating rotor mode, the width scale

factor for the streamlines was reduced by 10 times compared to the non-rotating rotor mode. If the width scale factor is not reduced, the streamlines will cover the entire domain of the hydroturbine. The pressure values at the end part of the hydroturbine are lower because the velocity values are higher at this part (Figure 8(b)).

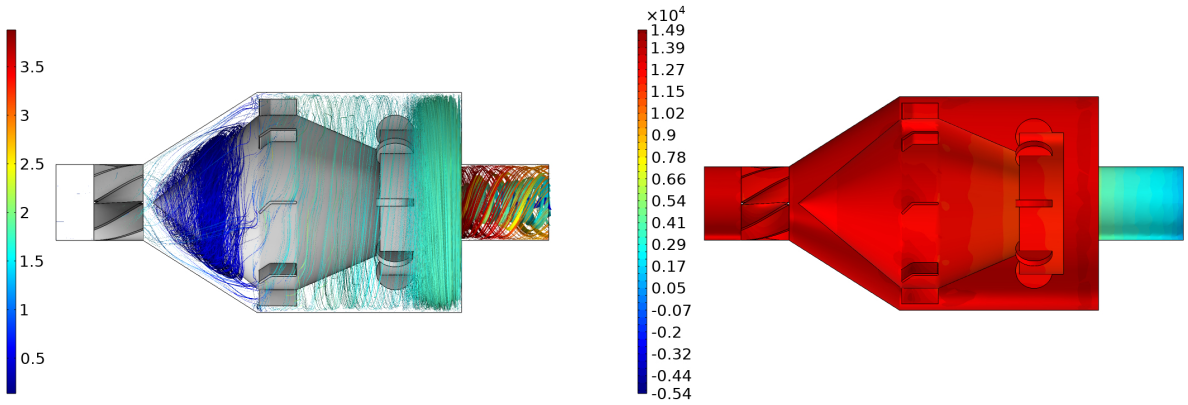

(a) (b)

Fig. 8. (a) Velocity streamlines (m/s) (b) Pressure distribution (Pa)

Figures 9(a) and 9(b) show the velocity slices for the non-rotating and rotating modes of the hydroturbine rotor, respectively.

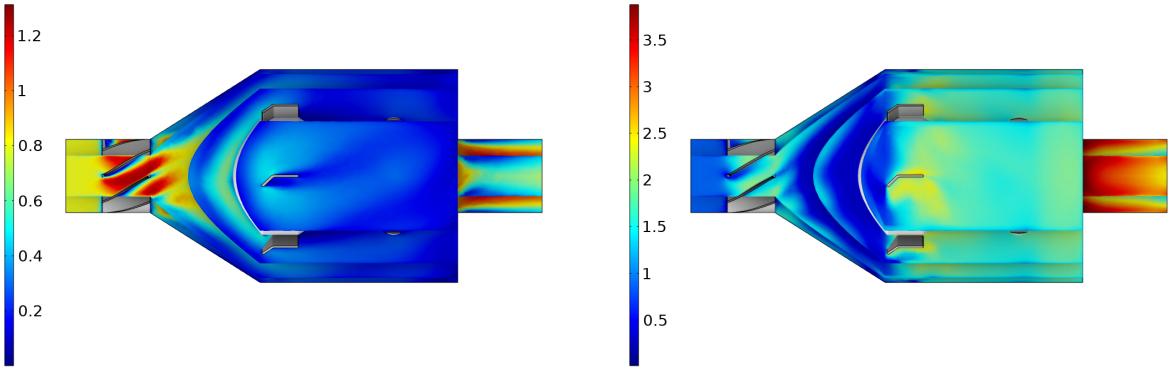

(a) (b)

Fig. 9. (a) Velocity slices (m/s) (b) Velocity slices (m/s)

3. Results

3.1 Experimental Studies

Figure 10(a) illustrates a general view of the hydroturbine used in the experimental tests. Figure 10(b) shows the experimental setup used during the studies. The experimental setup consists of the hydroturbine, reservoir, magnet wire, pump, ball valve, tachometer, ammeter, multimeter and pipes. The pump draws water from the reservoir and conveys it to the hydroturbine through the pipe. The water flow drives the rotation of the hydroturbine rotor, and the water that has traversed the hydroturbine is then returned to the reservoir through the pipe.

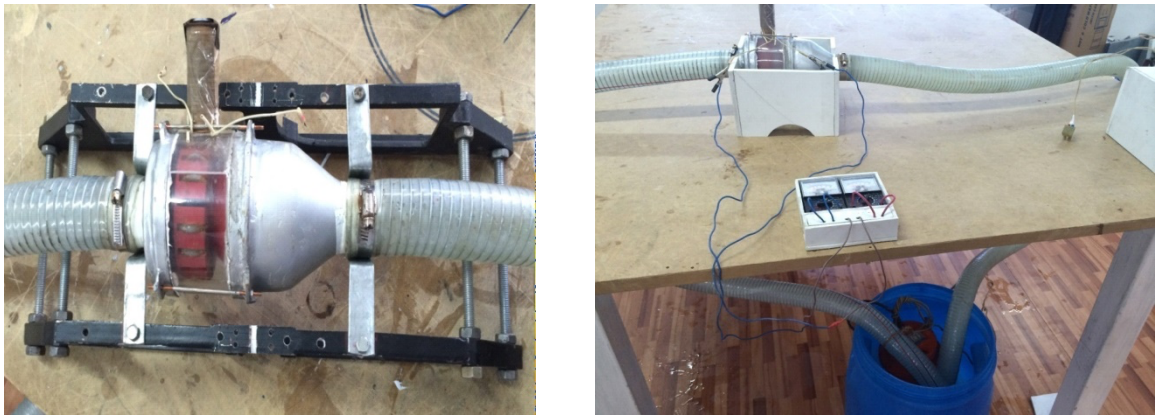

(a) (b)

Fig. 10. (a) Hydroturbine (b) Experimental setup

Table 3 shows the results of the experimental studies conducted on the hydroturbine. As the experimental study shows, the hydroturbine functions continuously through the complete range of alterations in water flow rate. Table 3 illustrates that by increasing the water discharge from 0.005 to 0.0062 m^3/s, the rotation speed changed only by 5 revolutions. This means that the hydroturbine reaches its peak performance in the eights experiment. A further increase in water discharge can lead to vibrations, and in some cases even to a hydraulic shock. By adjusting the water flow rate using a ball valve, the tachometer is employed to measure the amount of the rotation of the hydroturbine rotor. The electric power generated by the rotation of the hydroturbine rotor is defined according to Ohm's law, as described by Griffiths [20].

Table 3
Hydroturbine performance data related to water flow rate

No.	Flow rate m^3/s	Velocity m/s	Revolutions Per minute	Angular velocity Rad/s	Electric power W
1	0.0013	0.16579	28	2.93215	0.5
2	0.0018	0.22955	55	5.75959	0.7
3	0.0022	0.28056	68	7.12094	1.4
4	0.0028	0.35708	80	8.37758	4.5
5	0.003	0.38258	95	9.94838	5
6	0.0042	0.53562	120	12.56637	6.2
7	0.005	0.63764	150	15.70796	8
8	0.0062	0.79067	155	16.23156	8.1

4. Conclusions

This paper presents a comprehensive analysis involving numerical calculations and experimental studies aimed at defining the optimal parameters of the hydroturbine.

Direct Numerical Simulation was used in a two-dimensional domain to analyse the blade design and determine the angle of attack of the flow. After determining the angle of attack of the flow, the direction of the swirler was set accordingly. The numerical calculation was used to determine the velocity magnitude and pressure distribution, as well as the lift and drag forces for different angles of attack of the flow.

The k-epsilon model was selected to simulate the three-dimensional mode. In the non-rotating mode, the water velocity was depicted using streamlines and slices to showcase the flow behaviour around the swirler and rotor. The streamlines clearly indicate a change in the direction of water flow

after passing around the swirler. The pressure distribution demonstrates a proportional decrease in pressure as the velocity value increases.

For modelling the rotating mode, the frozen rotor approach was chosen. This method was used to calculate performance parameters such as head, torque, hydraulic power, hydroturbine power, and efficiency numerically.

During the experimental studies, performance data for the hydroturbine concerning water flow rate was gathered. These experiments involved adjusting the water flow rate using a ball valve, conducted across eight different experiments. The optimal operational state for the hydroturbine was determined during the eighth experiment, marking its peak performance. However, increasing the water flow rate beyond this optimal point could potentially lead to vibrations and a decrease in the rotor speed. For each flow rate, the revolutions per minute and angular velocity of the rotor were established. Additionally, the electric power generated in the magnet wire of the hydroturbine was calculated.

Numerical modelling allows for the determination of optimal parameters for the hydroturbine, thereby offering a way to reduce the financial costs associated with developing experimental prototypes. Simultaneously, the conducted 2D and 3D modelling and calculations can validate the effectiveness of the designed prototype. This innovative design is particularly valuable in tropical climates where water remains unfrozen, enabling these devices to operate throughout the year. Additionally, this hydroturbine aligns with modern global trends that prioritize environmentally friendly practices, as it avoids ecosystem disruption caused by activities like dam construction.

Acknowledgement
This research was funded by a grant from Committee of Science of the Ministry of Science and Higher Education of the Republic of Kazakhstan (Grant No. AP19677859 for 2023-2025).

References

[1] Dametew, Alie Wube. "Design and analysis of small hydro power for rural electrification." *Global Journal of Researches in Engineering* 16, no. 6 (2016): 234-241.

[2] Anyaka, B. O., and C. I. Imaeka. "Small Hydropower Projects for Rural Electrification in Nigeria. A Developer's Perspective." *International Journal of Innovative Technology and Exploring Engineering (IJITEE) ISSN* 3, no. 5 (2013): 2278-3075.

[3] Igbinovia, S. O., and P. E. Orukpe. "Rural electrification: the propelling force for rural development of Edo State, Nigeria." *Journal of Energy in Southern Africa* 18, no. 3 (2007): 18-26. https://doi.org/10.17159/2413-3051/2007/v18i3a3383

[4] Musa, Masjuri, Juhari Ab Razak, Musthafah Mohd Tahir, Imran Syakir Mohamad, and Md Nazri Othman. "Small scale hydro turbines for sustainable rural electrification program." *Journal of Advanced Research in Fluid Mechanics and Thermal Sciences* 49, no. 2 (2018): 138-145.

[5] Jabbar, Tahseen Ali, Rafi Mohammed Qasim, Safaa Hameed Faisal, and Bassam Abdullah Mohammed. "Investigating the Turbulent Flow around Semi-Circular Cylinder." *Journal of Advanced Research in Fluid Mechanics and Thermal Sciences* 112, no. 2 (2023): 191-213. https://doi.org/10.37934/arfmts.112.2.191213

[6] Alshqirate, Abed Alrzaq, Dastan Zrar Ghafoor, and Sachin L. Borse. "CFD Analysis of Flow Over Pickup Truck with And Without Covering Cargo Area Using OpenFOAM." *Journal of Advanced Research in Fluid Mechanics and Thermal Sciences* 90, no. 1 (2022): 40-51. https://doi.org/10.37934/arfmts.90.1.4051

[7] Jaafar, Reham K., M. A. Abdelrahman, Mina G. Mourad, Adnan A. Ateeq, and M. Moawed. "Modified Trailing Edge Impact on the Aerodynamic Performance of Wind Turbine Airfoil." *Journal of Advanced Research in Fluid Mechanics and Thermal Sciences* 91, no. 2 (2022): 133-144. https://doi.org/10.37934/arfmts.91.2.133144

[8] Pope, Stephen B. "Turbulent flows." *Measurement Science and Technology* 12, no. 11 (2001): 2020-2021. https://doi.org/10.1088/0957-0233/12/11/705

[9] Yusuf, Siti Nurul Akmal, Yutaka Asako, Nor Azwadi Che Sidik, Saiful Bahri Mohamed, and Wan Mohd Arif Aziz Japar. "A short review on rans turbulence models." *CFD Letters* 12, no. 11 (2020): 83-96. https://doi.org/10.37934/cfdl.12.11.8396

[10] COMSOL Multiphysics Version 5.4 CFD User's Guide.
[11] Liang, Chua Bing, Akmal Nizam Mohammed, Azwan Sapit, Mohd Azahari Razali, Mohd Faisal Hushim, Amir Khalid, and Nurul Farhana Mohd Yusof. "Numerical simulation of aerofoil with flow injection at the upper surface." (2021).
[12] Turalina, Dinara, and Daniyar BOSSINOV. "Theoretical and experimental investigations to define optimal parameters of the straight-flow turbine for non-dam hydro power station." *European Journal of Technique (EJT)* 8, no. 1 (2016): 1-12. https://doi.org/10.36222/ejt.467916
[13] Wilcox, David C. *Turbulence modeling for CFD*. Vol. 2. La Canada, CA: DCW industries, 1998.
[14] Paul, Edward L., Victor A. Atiemo-Obeng, and Suzanne M. Kresta. *Handbook of industrial mixing*. NY: Wiley-Blackwell, 2004. https://doi.org/10.1002/0471451452
[15] Morrison, Faith A. *An introduction to fluid mechanics*. Cambridge University Press, 2013. https://doi.org/10.1017/CBO9781139047463
[16] Yang, Shijie, Puxi Li, Zhaoheng Lu, Ruofu Xiao, Di Zhu, Kun Lin, and Ran Tao. "Comparative evaluation of the pump mode and turbine mode performance of a large vaned-voluted centrifugal pump." *Frontiers in Energy Research* 10 (2022): 1003449. https://doi.org/10.3389/fenrg.2022.1003449
[17] Sritram, Piyawat, and Ratchaphon Suntivarakorn. "Comparative study of small hydropower turbine efficiency at low head water." *Energy Procedia* 138 (2017): 646-650. https://doi.org/10.1016/j.egypro.2017.10.181
[18] Maulana, Muhammad Ilham, Ahmad Syuhada, and Rizki Kurniawan. "Experimental study on the effect of flow rate on the performance of two-blade archimedes screw turbine." *Journal of Advanced Research in Fluid Mechanics and Thermal Sciences* 61, no. 1 (2019): 10-19.
[19] Aziz, Muhammad Qamaran Abdul, Juferi Idris, and Muhammad Firdaus Abdullah. "Experimental study on enclosed gravitational water vortex turbine (GWVT) producing optimum power output for energy production." *Journal of Advanced Research in Fluid Mechanics and Thermal Sciences* 95, no. 2 (2022): 146-158. https://doi.org/10.37934/arfmts.95.2.146158
[20] Griffiths, David J. *Introduction to electrodynamics*. Cambridge University Press, 2023. https://doi.org/10.1017/9781009397735